PERGAMON

International Journal of Heat and Mass Transfer 44 (2001) 733–751

International Journal of HEAT and MASS TRANSFER

www.elsevier.com/locate/ijhmt

Lateral freezing of an anisotropic porous medium saturated with an aqueous salt solution

M. Song [a], R. Viskanta [b,*]

[a] *Department of Mechanical Engineering, Dongguk University, Seoul 100-715, South Korea*
[b] *School of Mechanical Engineering, Purdue University, Heat Transfer Laboratory, 1288 Mechanical Engineering Building, West Lafayette, IN 47907-1288, USA*

Received 21 May 1999; received in revised form 7 April 2000

Abstract

Lateral freezing of a porous medium saturated with an aqueous salt solution was investigated experimentally and theoretically to obtain the improved understanding of the solute redistribution during solid/liquid phase change. The emphasis was on the interaction between hydrodynamics and transport of energy and species in the solidifying and unsolidified regions and on the effect of the flow characteristics possessed by the porous matrix and dendrite arrays. Freezing experiments were performed in a square cross-section enclosure chilled and heated from the side by imposing uniform but different temperatures, and filled with the artificial porous structure. The latticed structure of the porous matrix phase and the shadowgraph enabled the flow visualization and the observation of the solidus and liquidus positions. Simultaneous measurements of local temperature and liquid composition at selected locations were also made. An analytical model based on heat and species conservation and relations from the phase diagram is suggested, and the predictions are compared with experimental data. The effect of porous matrix permeability was examined over a wide range of parameters by performing numerical experiments. The porous matrix phase affected the freezing of an aqueous salt solution by offering an additional resistance to the motion of the fluid and migration of separated crystals. The amount of macrosegregation was found to be mainly controlled by the porous matrix permeability in the direction of gravity. Macrosegregation was decreased when the permeabilities of the porous matrix phase and/or dendrite arrays were decreased.

1. Introduction

Solidification of a liquid saturated porous medium occurs in a wide variety of situations in geophysics and engineering. Examples include seasonal freezing of soil, artificial freezing of ground as a construction technique for supporting poor soils, insulation of underground buildings, latent heat of fusion thermal energy in porous media, and production and storage of frozen foods [1]. Metallurgical applications include manufacturing of composite materials and purification of metals, and biomedical applications include cryopreservation and banking of biological cells and tissues [2].

While the solidification of a mixture without the porous matrix phase has received considerable research attention, very few works have been reported on the subject of alloy solidification in the presence of porous matrix phase. The literature dealing with the freezing of a pure liquid saturated

* Corresponding author. Tel.: +1-765-494-5632; fax: +1+765-494-0539.
E-mail address: viskanta@ecn.purdue.edu (R. Viskanta).

0017-9310/01/$ - see front matter
PII: S0017-9310(00)00132-0

Nomenclature

C	concentration of solute, wt%
c_p	specific heat, J/(kg K)
D	diffusion coefficient of NH_4Cl in water, m^2/s
$\overrightarrow{\mathbf{Da}}$	volume average interfacial force exerted on liquid, N/m^3
G	local temperature gradient, K/m
h	total enthalpy, J/kg
K	permeability, m^2
k	thermal conductivity, W/(m K)
L	specific latent energy difference between liquid and ice phases, J/kg
M	specific latent energy difference between primary solid and ice phases, J/kg
m	slope of liquidus in phase diagram
N	specific latent energy difference between eutectic solid and ice phases, J/kg
P	pressure, Pa
$\mathbf{R}$	flow resistance coefficient
S_Q	segregation quotient in Eq. (29)
T	temperature, °C
t	time, s
x	horizontal coordinate, m
y	vertical coordinate, m
V	volume or growth velocity, m^3 or m/s
$\vec{\mathbf{v}}$	filtration velocity, m/s
β	volume expansion coefficient, /K
γ	surface energy, J/m^2
ε	volume fraction
η	dimensionless vertical coordinate, y/H
λ	primary dendrite arm spacing, m
μ	dynamic viscosity, N s/m^2
ξ	dimensionless horizontal coordinate, x/H
ϕ	angle between primary dendrite and positive x-direction
ρ	density, kg/m^3

Subscripts

e	eutectic solid phase
eff	effective value
in	initial value
l	liquid phase
s	solid phase
α	primary solid phase
∥	parallel direction with primary dendrite arm
⊥	normal direction to primary dendrite arm

porous medium is abundant and an extensive review is available [1]. Therefore, the review of previous research focuses on the few studies devoted to the phase change of solution saturated porous medium.

Cao and Poulikakos [3] experimentally investigated the downward solidification of aqueous ammonium chloride solution saturating the packed bed of glass beads. As the initial compositions tested were on the water rich side of the eutectic composition, the distribution of the liquid density destabilized the fluid motion both thermally and solutally. Disagreements between measured and predicted interface locations were attributed to the neglect of fluid motions in the theoretical model. Okada and Murakami [4] and Matsumoto et al. [5] studied the solidification of porous medium saturated with aqueous sodium chloride solution from a vertical side wall in a rectangular test cell. The solutal and thermal buoyance forces augment each other as the liquid in the mushy region is colder and richer in NaCl (and thus heavier) compared with the initial solution. In the analysis, the buoyancy driven convection resulting from both the temperature and concentration gradients was taken into account. The permeability of the mushy region, where the liquid phase coexists with the porous matrix (glass beads) and ice crystals, was evaluated through the simple relation in which the ratio of the permeability in the mushy region to that in the unsolidified region is some power of the ratio between the volume fractions of the liquid and void among the glass beads. The predicted distributions of the temperature and liquid concentration were strongly dependent on the value of the exponent in the permeability model, and good agreement with experimental data was obtained when the value of the exponent was 14. Upward solidification of aqueous NaCl solution saturated packed beds of glass beads has been investigated by Song et al. [6]. As the flow field was both thermally and solutally stable, the energy and species transport equations employed in the mathematical model were of the diffusion type. The behavior of the dimensionless temperature under different initial temperature and concentrationconditions could be explained by the relation between the local freezing rate and nonequilibrium undercooling. Choi and Viskanta [7] reported the experimental results under the same physical situation except that the system was cooled through the top surface and heated at the bottom. The experimental data of simultaneously measured temperature and concentration in the mushy region also confirmed that the undercooling due to the deviation from the phase equilibrium can be as large as several degrees Celsius despite the slow freezing rate encountered during the solidification of the nonmetallic alloys. Okada et al. [8] conducted an experimental and

theoretical study of the downward and lateral freezing of a packed bed of glass beads saturated with an aqueous sodium chloride solution, which was initially undercooled. The convective motion of the interdendritic liquid significantly influenced the growth velocity of solid phase under the tested conditions.

Studies on the solidification of an alloy in the presence of a porous solid matrix phase concerned with the opposing thermal and solutal buoyancy forces or dealing with the anisotropic flow characteristics of the porous matrix phase could not be identified in the literature.

The present paper reports on an experimental and theoretical investigation of the lateral freezing of a porous medium saturated with an aqueous salt solution. Major attention was directed to the influence of the porous matrix phase on the interaction of hydrodynamics and advective heat and species transfer and on the solute redistribution during phase change. The difficulty in the flow structure visualization, which is common in the experiments involving a porous medium, was resolved by the latticed structure of the porous matrix, and the monitoring of the liquid composition at multiple locations were performed by utilizing the experimental diagnostics based on the electrochemical principles.

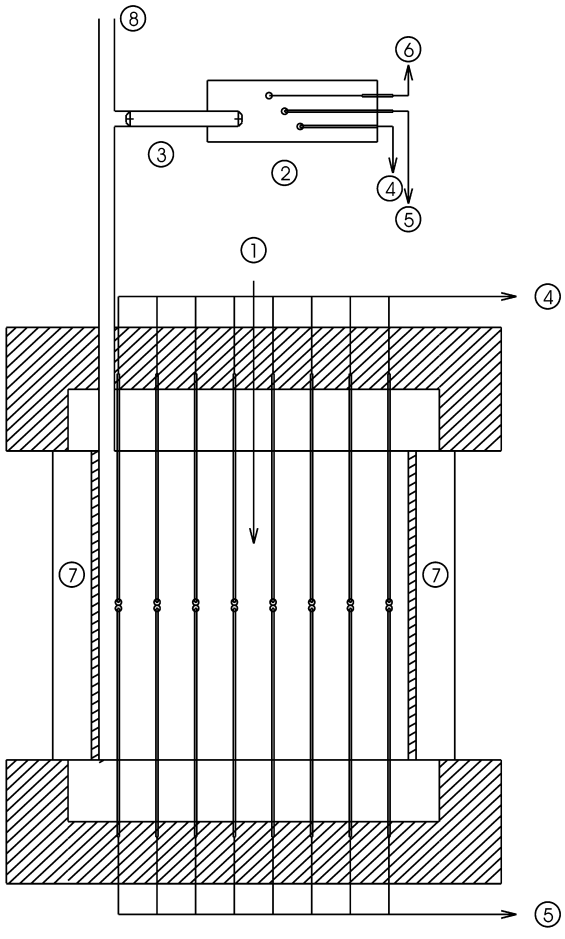

Fig. 1. Schematic diagram of experimental apparatus: 1. test cavity; 2. reference cavity; 3. salt bridge; 4. data logger (thermocouples); 5. data logger (concentration probes); 6. data logger (chloriding electrode); 7. heat exchanger; 8. overflow port.

2. Experiments

2.1. Test cell and porous matrix

Solidification of a porous medium saturated with an aqueous salt solution was made to occur within the square cross-section test cavity having the dimensions of 148 mm height and width and 74 mm depth. The sketch of the test cell assembly is shown in Fig. 1.

The vertical end walls were 6 mm thick copper plates of heat exchangers and served as the hot and cold walls. Ethyl alcohol (200 proof) was circulated from the constant temperature bath through the channels formed by the outer surface of the copper plates and the passages milled in the 33 mm thick carbon plastic (Lexan) blocks. Each heat exchanger, which is an assembly of a copper plate and a machined carbon plastic block, had three coolant passages which extended over the upper, middle and lower thirds of the copper plates. The vertical front and back walls and the horizontal top and bottom walls were made of 25 mm thick acrylic plates.

All the acrylic walls were covered with 25 mm thick Styrofoam insulation during the test run except for the brief moments of visualization. When the insulation was removed for the visual access, the convective air motion at the outer surfaces of the front and back walls was needed to be minimized to prevent condensation of the moisture in the ambient air and to maintain the thermal insulation. A pair of 3 mm thick glass plates was placed outside the Styrofoam layers which covered the front and back walls. During the visual access, only the central square portion of the insulation (148mm $\times$ 148 mm large) was removed so that the gaps between the glass and acrylic plates were kept sealed with the remaining Styrofoam. The glass plate at the back wall was translucent to serve as the diffusing screen for the shadowgraph images. Liquid-tight holes to allow for the insertion of thermocouples, concentration probes and filling/draining lines were placed in the top and bottom walls. The entire test assembly, including the test cell, heat exchangers and the insulation, was placed on an aluminum frame with leveling screws.

The porous matrix, which occupied the test cavity, was a rectangular latticed framework of evenly

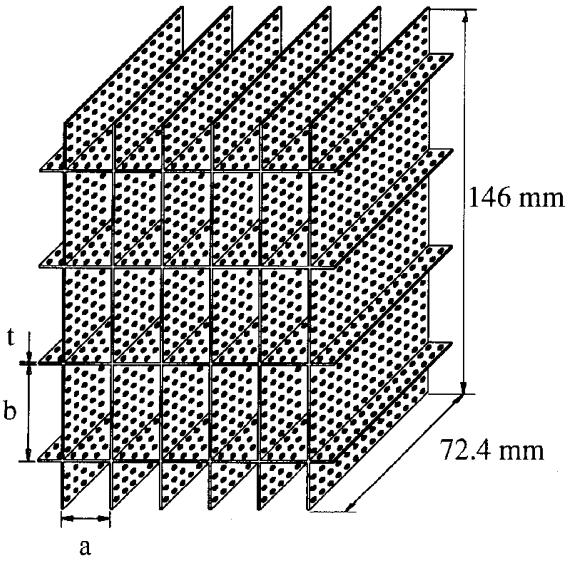

Fig. 2. Configuration of the porous matrix (see Table 1 for the values of a, b and t).

spanned permeable plates which were either perpendicular or parallel to the heat exchanging end walls (Fig. 2). The permeable plates were 3.18 mm thick perforated Polypropylene plates chosen among the few commercially available materials (distributed by McMaster-Carr Supply Co.). The perforated holes which provided about 25% open areas were staggered-centered, 2.38 mm in diameter, 4.76 mm in spacing, and were aligned to allow for the insertion of probes. The macroscopic characteristics of the porous media such as the porosities and permeabilities depended on the spacings of the permeable plates and are given in Table 1. The detailed explanation about the porous matrix configurations and the measurements of the macroscopic flow characteristic are given by Song and Viskanta [9].

2.2. Phase change material

The void of the porous matrix phase within the test cavity was filled with 27 wt% ammonium chloride aqueous (H_2O–NH_4Cl) solution, which has been used as a phase-change material in numerous previous solidification studies owing to the well established property data base and the manageable range of phase-change temperature [10]. The phase change process of aqueous ammonium-chloride solution is briefly reviewed to describe the terminology for the phases and regions adopted in the current study.

Table 1
Characteristics of porous structures ($K_o = 8.37 \times 10^{-9} m^2$)

Porous structure	a (mm)	b (mm)	ε_m	K_o/K_x	K_o/K_y
I	no porous structure				
II	36.4	18.2	0.256	0.116	0.208
III	18.2	18.2	0.199	0.232	0.232

The H_2O–NH_4Cl mixture is a simple eutectic system with eutectic temperature of $-15.4°C$ and eutectic composition of 19.7 wt% NH_4Cl, i.e., the two constituents neither combine to produce a compound nor form a solid solution but are miscible in all proportions in the liquid phase [11]. Two different types of solidification are recognized. The solidification of a liquid at a eutectic composition resembles that of a pure substance in some respects. The net rejection of species is absent at the macroscopically smooth solidification front, and the phase change temperature is fixed at a discrete value (eutectic temperature). Solidification of an off-eutectic composition aqueous ammonium chloride solution differs significantly from that of pure substances or that of eutectic composition liquid and is characterized by the dependence of the solidification temperature on the liquid concentration and by the solubility difference between the liquid and solid phases. When the aqueous ammonium chloride solution of concentration greater than the eutectic (hyper-eutectic) composition solidifies, solid NH_4Cl forms and water is rejected into the liquid phase at the solid/liquid interface. In the immediate vicinity of the solid/liquid interface, the rejected species build up to change the interfacial liquid concentration closer to eutectic composition. The liquid in front of the moving interface is undercooled and the resulting morphological instability leads to a pattern formation. Among the most common modes of crystal growth are the dendritic patterns in which tree like microscopic structures develop over a volume having the much larger spatial extents than the length scales of the array of the dendrites [12]. This region is called the mushy region and is usually treated as a porous medium in the macroscopic solidification models. The temperature of the liquid in the mushy regioncan be significantly lower than what is depicted by the liquidus of the equilibrium phase diagram due to the presence of undercooling.

The solid phase forming at eutectic composition is distinguished from the solid phase forming from an off-eutectic liquid. The former is referred to as eutectic solid phase, which is a finely mixed composite of ice and solid NH_4Cl and forms at the colder boundary of the mushy region. The latter is referred to as primary solid phase, as it precipitates at the temperature higher than eutectic temperature along the liquidus of the phase diagram, mainly within the mushy region. When the solidification of a mixture in a saturated porous medium is considered, there is an additional solid

phase consisting of the solid matrix of a porous medium, namely the porous matrix phase.

During the solidification of the porous medium initially saturated with an off-eutectic liquid alloy, three distinct regions are found: the already solidified, the unsolidified, and the solidifying region. Throughout the discussion, these three regions will be referred to as the solid, liquid and mushy regions according to the entities occupying the void of the porous matrix phase. Therefore, the solid region is composed of the porous matrix, primary solid and eutectic composition solid phases, and the mushy region is composed of the porous matrix, primary solid and liquid phases, while the liquid region has only porous matrix and liquid phases. The thermophysical properties of all phases are presented in Table 2.

The boundaries between the liquid and mushy regions and between the mushy and solid regions will be referred to as liquidus and solidus interfaces, as these boundaries confine the regions where no solid phase or liquid phase exist.

2.3. Test procedure

The preparation of each experiment included: (1) the assembly of the test cell with the porous structure inside, (2) saturation of the porous matrix with the aqueous NH_4Cl solution of the predetermined concentration, and (3) establishment of the uniform initial temperature condition.

The solution of the predetermined concentrations (27 ± 0.02 wt% NH_4Cl) was obtained by mixing deionized water of a resistivity larger than 15 Mohm-cm with a requisite amount of research-grade ammonium chloride grains (manufactured by J.T. Baker Inc.). In order to avoid entrapment of air bubbles in the small pores of the porous structure and blocking the flow passages, the solution was degassed and slowly (0.6 cm^3/s) siphoned into the test cavity. The initial uniform temperature condition was reached by controlling the temperatures of both end walls. Due to the poor heat transfer rate dominated by conduction, there was a difficulty in attaining the uniform temperature profile within a reasolable time period by simply maintaining the wall temperatures at the predetermined initial temperature, especially when the initial temperature was lower than the room temperature. Therefore, the wall temperatures were set a few degrees below the predetermined initial temperature at first, and were later readjusted to be the same as the center temperature of the test cavity when it reached the predetermined initial temperature (which took about 10 h). The desired uniformity (initial temperature $\pm 1^\circ C$) was reached within several more hours, but the initial temperature obtained in this manner had to be a few degrees higher than the equilibrium liquidus temperature of the initial solution since the wall temperature must be higher than the liquidus temperature of the initial solution all the time.

The heat exchangers were connected to two constant temperature baths (NESLAB ULT-80DD for the cold coolant and HAAKE A82 for the hot coolant) through a valve system. The temperature of the hot wall was maintained at the initial temperature throughout the run, while the cold wall temperature was rapidly dropped to initiate the solidification of the porous medium within the test cavity. A 0.1 hp booster pump (Cole-Parmer L-07002-72) was installed on the discharge side of the cold temperature bath to increase the coolant flow rate. The cold wall temperature reached the desired value in less than 4 min with the cold bath temperature $10^\circ C$ below the desired cold wall temperature. With the help of the booster pump, the center temperature of the cold heat transfer surface was maintained within $\pm 1^\circ C$ of the desired temperature. The uniformity of temperature on the heat transfer surface was insured with the five thermocouples, placed close to the test cavity along the centerline of each copper plate, as the heat transfer rates between the phase change medium and copper plates were noticeably nonuniform along the height. The coolant flow rate in the passages in the upper third of the cold wall was adjusted to be larger than that of the

Table 2
Thermophysical properties of each phase

Phase	Liquid	Solid NH_4Cl	Ice	Eutectic solid	Porous matrix
ρ	1082	1530	920	998	910
c_p	3324	1496	1950	1861	1520
k	0.408	2.5	2.0	2.1	0.22
L, M or N	333.7	68.7	0	13.5	0
μ	1.43×10^{-3}				
D	1.0×10^{-9}	0	0	0	
β	3.23×10^{-4}				
β	-0.279				

coolant passage in the middle, while the flow rate of the lower passage was adjusted to be smaller than in the middle coolant passage. The opposite adjustment was needed for the coolant flow rates of the hot wall, but the amount of adjustment was smaller. With the adjustments of the flow rate made manually and intermittently, it was possible to maintain the temperature distribution along the height of the hot and cold walls within $\pm 0.5^{\circ}C$ of the wall-center temperature during the first 30 min of solidification and within $\pm 0.2^{\circ}C$ afterwards.

Measurements of the temperatures inside the test cavity were made with type-T thermocouples, calibrated within an accuracy of $\pm 0.1^{\circ}C$. Due to the highly corrosive nature of the aqueous NH_4Cl solution, the copper and constantan lead wires were sheathed by a 1.65 mm O.D. stainless steel tube, and the thermocouple bead was grounded inside the closed end of the sheathing tube (Omega TMQSS-62). Measurements of the local liquid concentrations in the liquid and mushy regions were made with the concentration probes which has an uncertainty of $\pm 2.5\%$ of the solute concentration reading. A probe to measure the local liquid concentration was a 0.8 mm O.D. silver wire electrically insulated from the solution by a 0.3 mm thick Kynar layer, except at the plain cut tip cross-section. As the electrochemical potential of the chloride ion in the solution is mainly determined by the local temperature and chemical composition, the local liquid concentration could be determined from the relative electric potential of the working electrode and the local temperature data measured with thermocouples. The simultaneous measurement of the temperature and liquid concentration is also preferred for the more accurate estimation of the local undercoolings. For each measuring position, a pair of temperature and liquid concentration probes were inserted from the opposite directions through the liquid-tight holes placed in the top and bottom walls, and the sensing tips were separated from each other with a gap less than 1 mm. A detailed discussion of the theory, fabrication, calibration and uncertainties of the concentration probe are found elsewhere [13].

The qualitative observations of the flow structures in the liquid region were made possible by the latticed arrangement of the porous structure and the shadowgraph technique utilizing the mercury arc lamp as a light source. The shadowgraph images of the test cavity were visualized on the translucent glass plate, which is the last component of the test cell assembly in the light path. The images were photographed at about 15, 30, 60, 120, 120, and 480 min after the initiation of cooling.

3. Analysis

3.1. Model equations

Consideration is given to the porous medium within a square cross-section cavity undergoing phase-change. The analysis assumes that the transport processes are two-dimensional and laminar. The thermophysical properties of all phases are assumed to be constant, but may differ from phase to phase. The solid phases are considered stationary and rigid. Also, the Boussinesq approximation is assumed to be valid for the buoyancy force term exerted on the liquid phase. Furthermore, it is postulated that the interfacial force exerted in the liquid phase by any of the solid phases can be represented by the D'Arcian expression. With the assumption of local thermal and phase equilibria and neglecting the viscous dissipation, the volume averaged transport equations utilizing the single domain approach [14] are as follows;

Continuity:

$$\frac{\partial \rho}{\partial t} + \nabla \cdot \left(\rho_\ell \vec{\mathbf{v}}\right) = 0 \tag{1}$$

Momentum:

$$\frac{\partial}{\partial t}\left(\rho_l \vec{\mathbf{v}}\right) + \nabla \cdot \left(\frac{\rho_\ell}{\varepsilon_\ell}\vec{\mathbf{v}}\vec{\mathbf{v}}\right) = -\varepsilon_\ell \nabla P + \nabla \cdot \left(\varepsilon_\ell \mu_{\ell,\,\mathrm{eff}}\right) + \varepsilon_\ell \vec{\mathbf{Da}} + \varepsilon_\ell \rho_\ell \vec{\mathbf{g}}\left[\beta_C (C_\ell - C_{\mathrm{ref}}) + \beta_T (T - T_{\mathrm{ref}})\right] \tag{2}$$

Energy:

$$\frac{\partial}{\partial t}(\rho c_{\mathrm{P}} T) + \nabla \cdot \left(\rho_\ell c_{P\ell} \vec{\mathbf{v}} T\right) = \nabla \cdot (k_{\mathrm{eff}} \nabla T) + \rho_\alpha (L - M)\frac{\partial \varepsilon_\alpha}{\partial t} + \rho_{\mathrm{e}} (L - N)\frac{\partial \varepsilon_\alpha}{\partial t} \tag{3}$$

Species:

$$\frac{\partial}{\partial t}(\rho C_\ell) + \nabla \cdot \left(\rho_\ell \vec{\mathbf{v}} C_\ell\right) = \nabla \cdot \left(\varepsilon_\ell \rho_\ell D_{\ell,\,\mathrm{eff}} \nabla C_\ell\right) + \frac{\partial}{\partial t}(\rho C_\ell - \rho C) \tag{4}$$

In the above equations, the subscripts ℓ, α, and e denote the liquid, primary solid and eutectic solid phases, respectively, and ε_k is the volume fraction of the phase k.

Since solidification is relevant to the physical phenomena occurring on different length scales ranging from atomic rearrangement to heat extraction at the system level [14], a macroscopic model requires constitutive relations, which depict microscale phenomena in

terms of the macroscopic variables. The term $\vec{\mathbf{Da}}$ in the momentum equation (Eq. (2)) represents the volume averaged force exerted on the unit volume of the liquid at the microscopic interface between the liquid and the other solid phases. During the solidification of the porous medium saturated with an off-eutectic composition solution, the porous matrix phase coexists with the liquid phase in the liquid region and it also coexists with the primary solid and the liquid phases in the mushy region.

The expected range of the filtration velocity is smaller than a few mm/s under the conditions considered in the present study. The linear relationship between the filtration velocity and the average interfacial force for the relatively small filtration velocities has been confirmed by numerous experimental and analytical studies since the original experiments on the flow of water through a packed sand by D'Arcy. When the linear relationship is valid, it can be shown using dimensional analysis that the relevant physical variables of the proportionality coefficient are the fluid viscosity and the characteristic lengths of the porous matrix, so that the average interfacial force is expressed as

$$\vec{\mathbf{Da}} = -\mu_\ell \mathbf{R}\vec{\mathbf{v}} \tag{5}$$

where $\mathbf{R}$ is the second order resistance tensor and is the inverse of the permeability. The model for $\mathbf{R}$ should depict the flow characteristics of the solid structure created by the superposition of the solid matrix and primary solid phases. Discussion concerning the flow characteristics of the porous matrix, formed by superposing arrays of solid particles having greatly different morphology, is premature. Research on the macroscopic transport characteristics of multidisperse medium is underway [15]. Under the assumption that the structure of the porous matrix is relatively coarse compared with that of the primary solid phase so that the size and shape of the pores are close to those of the pores formed only by the primary solid phase and are little affected by the existence of the porous matrix phase (except that the pore velocity is increased by the factor of $1/(1-\varepsilon_m)$, the resistance tensor for the medium simultaneously occupied by the primary solid and porous matrix phases as well as the liquid phase is determined from

$$\mathbf{R} = \max\left\{\mathbf{R}_m, |\mathbf{R}_\alpha|/(l-\varepsilon_m)\right\} \tag{6}$$

where $\mathbf{R}_m$ and $\mathbf{R}_\alpha$ account for the flow resistance offered by the porous structure and the primary solid phase, respectively. The maximum value operator is intended to insure smooth change when the liquidus interface is passing the local medium.

The resistance tensor of the porous matrix phase in the absence of the other solid phases is defined as

$$\mathbf{R}_m = \begin{bmatrix} R_{x,m}/K_o & 0 \\ 0 & R_{y,m}/K_o \end{bmatrix} \tag{7}$$

where the coefficients $R_{x,m}$ and $R_{y,m}$ are

$$R_{x,m} = K_o/K_{x,m} \tag{8}$$

$$R_{y,m} = K_o/K_{y,m} \tag{9}$$

The empirically determined values of $R_{x,m}$, $R_{y,m}$ and K_o for the present porous structures are given in Table 1. In the numerical experiments, the effect of porous matrix flow characteristics on the predicted results was investigated by varying the values of coefficients $R_{x,m}$ and $R_{y,m}$.

The resistance tensor of the primary solid phase in the absence of the porous matrix phase in terms of the interdendritic permeabilities is given by

$$\mathbf{R}_\alpha = \begin{bmatrix} \sin^2\phi\dfrac{1}{K_\perp} + \cos^2\phi\dfrac{1}{K_\parallel} & \sin\phi\cos\phi\left(\dfrac{1}{K_\parallel} - \dfrac{1}{K_\perp}\right) \\ \sin\phi\cos\phi\left(\dfrac{1}{K_\parallel} - \dfrac{1}{K_\perp}\right) & \cos^2\phi\dfrac{1}{K_\perp} + \sin^2\phi\dfrac{1}{K_\parallel} \end{bmatrix} \tag{10}$$

In the above equation, ϕ is the angle between the primary dendrite and the positive x-axis. It is assumed that the direction of primary dendrite arms is determined at the beginning of the primary solid formation and parallel with the direction of the local temperature gradient. Permeabilities in the parallel ($K_\parallel$) and normal ($K_\perp$) directions to the primary dendrites are determined from the liquid volume fraction and the primary arm spacing through the following equations, which are adopted from Felicelli et al. [16]:

$$K_\parallel = 7.425\times10^{-}\lambda_1^2\left\{\ln\frac{1}{1-\varepsilon_n} - 1.487 + 2(1-\varepsilon_n) - \frac{(1-\varepsilon_n)^2}{2}\right\} \tag{11}$$

$$K_\perp = \max\left\{\lambda_1^2\left[5.563\times10^{-2}\left(\frac{\varepsilon_n}{1-\varepsilon_n}\right)^{0.25} - 5.955\times10^{-2}\right]2.104\times10^{-3}\lambda_1^{2.08}\varepsilon_n^{3.32}\right\} \tag{12}$$

In the above equations, ε_n is the modified liquid volume fraction considering the presence of the porous matrix phase and is defined as

$$\varepsilon_{\mathrm{n}} = \varepsilon_{\ell}/(1-\varepsilon_{\mathrm{m}}) \tag{13}$$

The detailed discussion of the flow characteristics of the columnar dendrite arrays is available in Poirier [17] and Felicelli et al. [16]. The theoretical models, which quantify the primary arm spacing as a function of growth rate, temperature gradient and local composition, have been developed and are presented in the metallurgy textbooks. The following equation which relates the primary arm spacing to the local temperature gradient (G), the growth velocity (V) and the local liquidus temperature (T_{liquidus}) is obtained by combining Eq. (9) of Somboonsuk et al. [18] and Eqs. (7), (8) and (10) of Trivedi [19],

$$\lambda_1^4 G^{\,2} V = -1344 \frac{\gamma D_{\ell} m (C_{\ell} - C_{\alpha}) T_{\mathrm{liquidus}}}{\rho (L - M)} \tag{14}$$

where γ is the surface energy of the interface between the liquid and primary phases, and m is the slope of liquidus line in the phase diagram. It is assumed that the local primary arm spacing is determined at the beginning of the primary solid formation and does not change unless complete remelting occurs and is followed by resolidification. Neither the empirical correlation nor the theoretical model which provides reliable values of secondary arm spacings during the solidification of NH_4Cl–H_2O system is available.

The macroscopic transport equations (Eqs. (1)–(4)) have the phase volume fractions (ε_k) as unknown variables, in addition to the main dependent variables such as $\vec{\mathbf{v}}$, P, T and C_{ℓ}. The other quantities can either be determined from these dependent variables or are given as the transport properties. Three additional relations are required to solve for ε_{ℓ}, ε_{α} and ε_{e} as m is specified and does not change. One of the relations is self-evident from the definition of the phase volume fraction:

$$\sum_k \varepsilon_k = 1 \tag{15}$$

The other two are obtained from the equilibrium phase diagram and constitute the phase-change model:

$$\varepsilon_{\alpha} = 0, \quad \varepsilon_{\mathrm{c}} = 0 \qquad \text{in liquid region} \tag{16}$$

$$T = mC_{\ell} + \delta_T, \qquad \varepsilon_{\mathrm{e}} = 0 \quad \text{in the mushy region} \tag{17}$$

$$T = T_{\mathrm{eut}}, \qquad C_{\ell} = C_{\mathrm{eut}} \quad \text{at solidus interface} \tag{18}$$

$$\varepsilon_{\ell} = 0 \quad \text{in solid region} \tag{19}$$

Only one relation is required for the solid region because liquid concentration need not be determined. The species equation for the solid region becomes

$$\frac{\partial}{\partial t}(\rho C) = 0 \tag{20}$$

The values of m and δ_T used in Eq. (17) are -87.11 and 1.76, respectively.

3.2. Thermophysical properties

The average density, composition and specific heat are defined as

$$\rho = \sum_k \varepsilon_k \rho_k \tag{21}$$

$$C = \frac{1}{\rho} \sum_k \varepsilon_k \rho_k C_k \tag{22}$$

$$c_{\mathrm{p}} = \frac{1}{\rho} \sum_k \varepsilon_k \rho_k c_k \tag{23}$$

Also, $\vec{\mathbf{v}}$ represents the filtration velocity, and L, M and N are the latent energy of phase ℓ, α and e, respectively.

The analytical determination of the effective diffusion coefficients, $\mu_{l,\,\mathrm{eff}}$, $D_{l,\,\mathrm{eff}}$ and k_{eff} are very complicated even for the simple geometries. As the predicted flow field is affected little by the moderate change in $\mu_{l,\,\mathrm{eff}}$, the effective viscosity is assumed to be the same as that of liquid phase. The effective diffusion coefficient for the NH_4Cl solute in the liquid phase ($D_{l,\,\mathrm{eff}}$) is assumed to be the same as that of the liquid solution since the diffusive transport of species is negligibly small compared with the advective transport. For the effective thermal conductivity, the volume weighted conductivity model (or parallel resistance model) defined below is utilized,

$$k_{\mathrm{eff}} = \sum_k \varepsilon_k k_k \tag{24}$$

Even though the transport equations allow for the spatial and transient changes of the phase densities as well as the discrete differences between them, the volume expansion or shrinkage due to the phase change and resulting fluid motion are assumed to be negligible:

$$\rho_{\alpha} = \rho_{\mathrm{e}} = \rho_{\ell} \tag{25}$$

At the bounding walls, the no-slip hydrodynamic boundary conditions and the null species flux conditions are imposed. The adiabatic boundary conditions were imposed at the top and bottom walls, and the vertical end walls were held at constant temperatures.

3.3. Method of solution

The governing transport equations (Eqs. (1)–(4)) are partial differential equations parabolic in time and elliptic in space coordinates. The numerical procedure based on the SIMPLEC [20] is used to predict the flow, temperature and liquid concentration fields. In obtaining the solution of descritized algebraic equations for the pressure correction, the polynomial preconditioned conjugate gradient (PPCG) numerical algorithm [21,22] is employed. To solve the algebraic equations for the velocities, temperature and liquid concentration fields, SIP [23] is employed as the coefficient matrices are not symmetric.

After the flow, temperature and liquid concentration fields are determined, the phase volume fractions are updated utilizing the phase-change model equations. The predictor–corrector type algorithm, which takes into account the direct coupling among the temperature, liquid concentration and phase volume fractions not only through the phase-change model equations but also through the energy and species equations, is developed and employed in the numerical implementation. In this algorithm, the phase volume fractions are updated in such a way that the nodal values of total enthalpy and average composition remain unchanged. At first, the nodal values of the total enthalpy and average composition per unit volume are calculated from the most recent values of temperature, liquid concentration and phase volume fractions using the following equation and Eq. (22):

$$\rho h = \rho c_p T + \varepsilon_\ell \rho_\ell L + \varepsilon_\alpha \rho_\alpha M + \varepsilon_e \rho_e N \tag{26}$$

Then, it is determined whether the control volume belongs to the solid region or not by comparing ρh to the total enthalpy of the fully solid medium $[(\rho h)_s]$ having the same average composition when the solidification has just completed ($T = T_{eut}$). For the control volumes which do not belong to the solid region, ρh is compared with the total enthalpy of the medium having the same average composition when the eutectic composition solid phase is about to form $[(\rho h)_m]$. If ρh is smaller than $(\rho h)_m$ and larger than $(\rho h)_s$, the solidus interface is passing through the control volume, and the phase volume fractions are calculated under the constraints for the solidus interface (Eq. (18)). For the control volumes which do not belong to either the solid region or the solidus interface, the phase volume fractions are calculated under the constraints for the mushy region (Eq. (17)).

At a given time step, the successive update of flow, temperature, liquid concentration and phase volume fractions are continued until two convergence criteria are satisfied. The first criterion requires that the relative changes in the average solid volume fraction of the system (ε_s) is smaller than 1×10^{-6}, which is defined as

$$\varepsilon_s = \left[\sum(\varepsilon_\alpha + \varepsilon_e)\nabla V\right] / \sum \nabla V \tag{27}$$

The second criterion requires that the largest value of the mass imbalances at the node control volumes be smaller than 1×10^{-6}. When the second criterion is satisfied, the maximum mass imbalance is smaller than the one caused by the error of 1×10^{-7} m/s in the filtration velocity.

For the results discussed in the paper, the calculation grid has 67×63 node points. The time step is about 1 s initially and is gradually increased using the relation

$$\Delta t = 0.0589(t + 288)^{0.5} \tag{28}$$

to insure that the changes in the dependent variables are small. For each time step advance, the change in the solid fraction of the system (ε_s) was smaller than 0.01% and the number of iterations needed for the converged solution ranged between 20 to 100. Calculation times ranged from 6,000 to 80,000 CPU seconds on a CYBER 205 computer for a simulation time of 8 h. Additional computational details can be found elsewhere [24].

4. Results and discussion

4.1. Experimental conditions

Solidification experiments were conducted for three different porous matrix configurations as well as for different combinations of hot and cold wall temperatures. Table 3 summarizes the experimental conditions which are discussed. Additional experimental results can be found elsewhere [24]. During the lateral solidification of a 27 wt% ammonium chloride aqueous solution, the thermal and solutal buoyancy forces oppose each other in the mushy region as the interdendritic liquid is colder and richer in water compared with the initial solution. Even though the change of the liquid density along the liquidus of equilibrium-phase dia-

Table 3
Experimental conditions

Experiment	Porous structure	T_h (°C)	T_c (°C)
1	I	20	−30
2	II	20	−40
3	II	40	−40
4	III	20	−40

gram is dominated by the solutal expansion, the flow in the mushy region is not unidirectionally upward, since it interacts with the flow in the liquid region (which is generally downward near the liquidus interface). The interaction of the momentum, energy and species transport with the separation, migration and growth of the equiaxed crystal also presents another and different aspect to the phenomenon from the lateral solidification of the hypoeutectic solution. The experimental studies on the lateral solidification of a hypereutectic aqueous ammonium chloride solution in the absence of a porous structure have been made and have revealed the nature of the double-diffusive transport process [25,26]. The discussion focuses on the transport features revealed by the newly developed concentration measuring diagnostics and the effect of the porous structure under different temperature conditions.

4.2. Experiment 1: absence of porous matrix

In Fig. 3 the shadowgraph images taken during Experiment 1 are shown, in which the porous structure was absent and the hot wall temperature was slightly higher than the equilibrium liquidus temperature of the initial solution (19.3°C). A large fraction of the primary solid phase initially formed on the vertical cold wall separated, migrated downward and stranded along the bottom wall, as the density of the NH_4Cl crystal is significantly larger than that of the liquid phase, and the initial fluid motion near the cold wall was downward driven by the thermal buoyancy force.

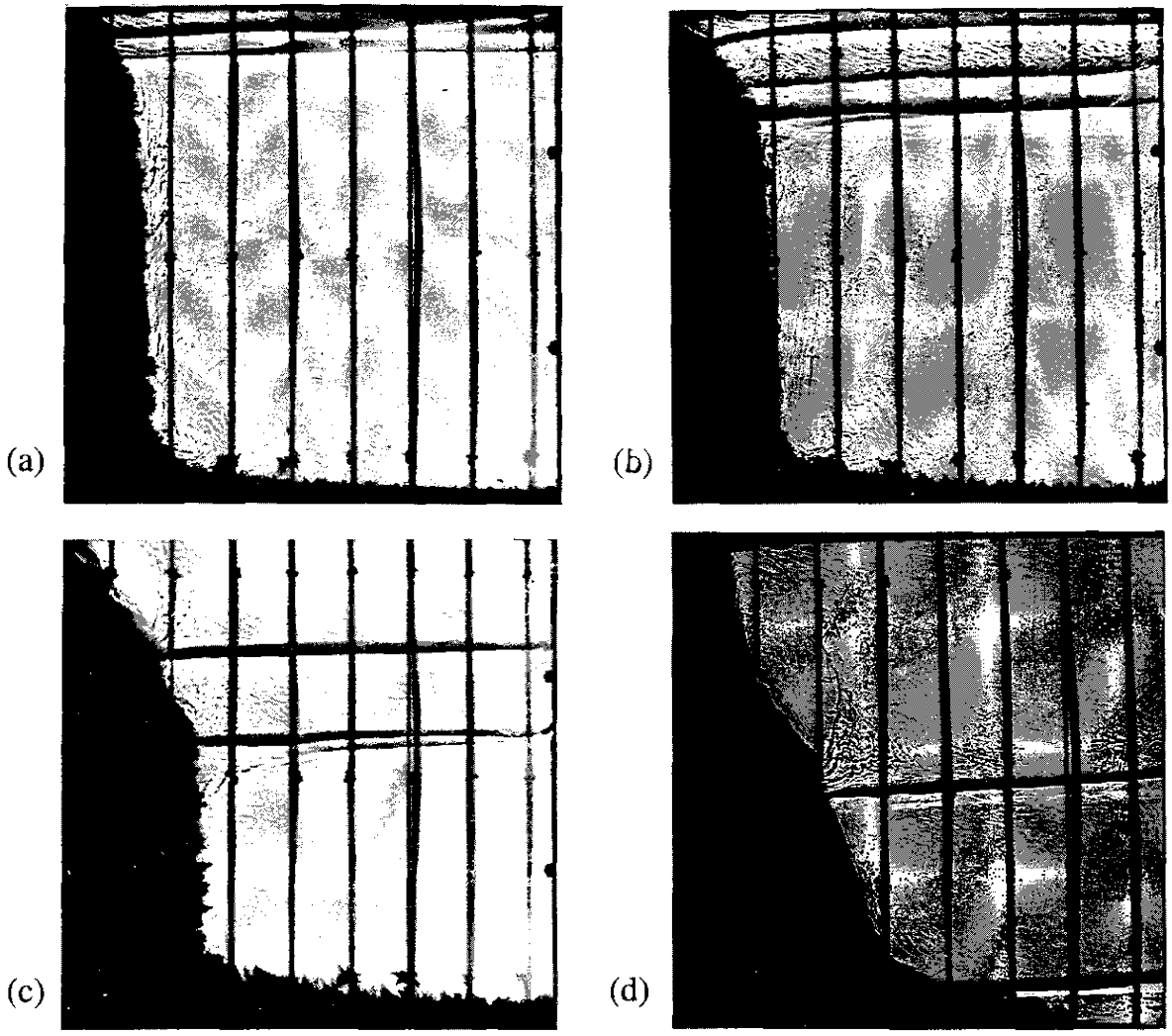

Fig. 3. Shadowgraph images taken during Experiment 1: (a) $t = 30$ min, (b) $t = 60$ min, (c) $t = 120$ min, and (d) $t = 480$ min.

At 15 min after the initiation of cooling, the separation of primary solid phase from the cold wall did not occur, and the columnar mushy region had developed past the measuring probes at $\xi = 0.07$. Judging from the configuration of the ascending plumes carrying the water-rich fluid, the solidification was intense in the mushy region along the bottom wall as well as near the cold wall. A number of crystals, small in size compared with the initially separated primary solid phase, were being ejected into the liquid region and were carried by the plumes [24]. After 30 min into the experiment (Fig. 3(a)), multiple pairs of dark and bright strips appeared near the top wall. Some of the large plumes, which emanated from the oblique liquidus interface, became distinguishable. Around the probe tips at $\eta = 0.07$ in the liquid region, growth of NH_4Cl crystals was observed. According to the temperature and the liquid concentration data shown in Figs. 3(a), the liquid around the measuring positionsat $\eta = 0.07$ and 0.50 was significantly undercooled (~3.5°C during the first three hours of the experiment). As the magnitudes of the undercooling at two different heights were not noticeably different, the seed crystals which triggered the growth of equiaxed dendrites around the probe tips near the bottom are considered not to have nucleated locally but to have originated from some remote site. The growth direction of the dendrites along the bottom wall was toward the cold wall and at the same time toward the top wall. At $t = 60$ min (Fig. 3(b)), the dark and bright strips near the top wall had separated into three distinct double diffusive interface (DDI) images. As these DDI moved, the first and the second highest ones merged ($t \approx 90$ min), and accordingly the liquid region was divided into three fluid layers. From this time on the number of fluid layers did not change throughout the experiment. The vertical extent of the upper and middle fluid layers kept on increasing as the lower DDI descended at the greater rate than the upper one (Fig. 3(c) and 3(d)).

The shapes of the plumes, which carried the water-rich fluid through the liquid region, were different from one fluid layer to the other. In the lower fluid layer, the major discharge of the interdendritic liquid was across the liquidus interface just below the upper bounding DDI, since the liquidus interface was almost vertical and the thermal flow was relatively weak (Fig. 3(c)). In the middle fluid layer, the discharge of the water-rich fluid was along the entire liquidus interface due to the slope of the interface. The downward distortion of the small diameter plumes was influenced by the thermal flow of intermediate strength. In the top fluid layer, the interdendritic liquid was discharged across the liquidus interface near the lower bounding DDI and was carried by relatively thick plumes associated with the channels. The water-rich fluid which reached the top portion of the upper fluid layer was redirected towards the cold wall and descended along the liquidus interface, drawn by the rather strong thermal flows. Note that remelting of the primary solid phase occurred near the upper left corner of the test cavity. The stronger thermal flow in the upper fluid layers was due to the larger temperature differences between the hot wall and the liquidus interface, which, in turn, was affected by the solutal stratification in the entire liquid region.

The temperature and liquid concentration data measured at $\eta = 0.07$ during Experiment 1 indicated that significant undercooling existed both in the liquid and mushy regions near the bottom [24]. The extent of the undercooling in the liquid region was fairly uniform and almost unchanged, as both of the temperature and liquid concentration were uniform and decreased continuously. The extent of the undercooling in the mushy region was close to that in the liquid region but tended to increase as the solidus interface was approached. At $\eta = 0.52$ (Fig. 4), the temperature and liquid concentration in the liquid region differed little from those at $\eta = 0.07$, when the measuring positions belonged to the lower fluid layer. This indicated that both the temperature and concentration distributions in the lower fluid layer were rather uniform. When the lowest DDI passed the measuring positions at $\eta = 0.52$, both the temperature and the liquid concentration in the liquid region decreased drastically. Since the liquid in the middle fluid layer was not undercooled, the equilibrium liquidus temperatures

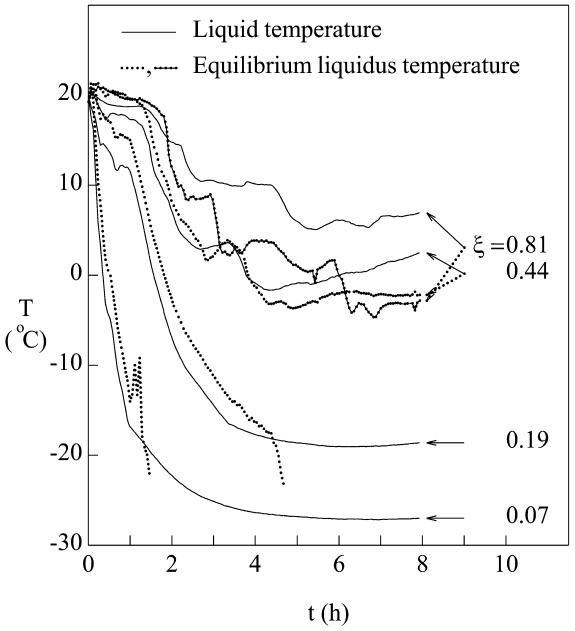

Fig. 4. Transient liquid and equilibrium liquidus temperature readings (Experiment 1) at $\eta = 0.52$.

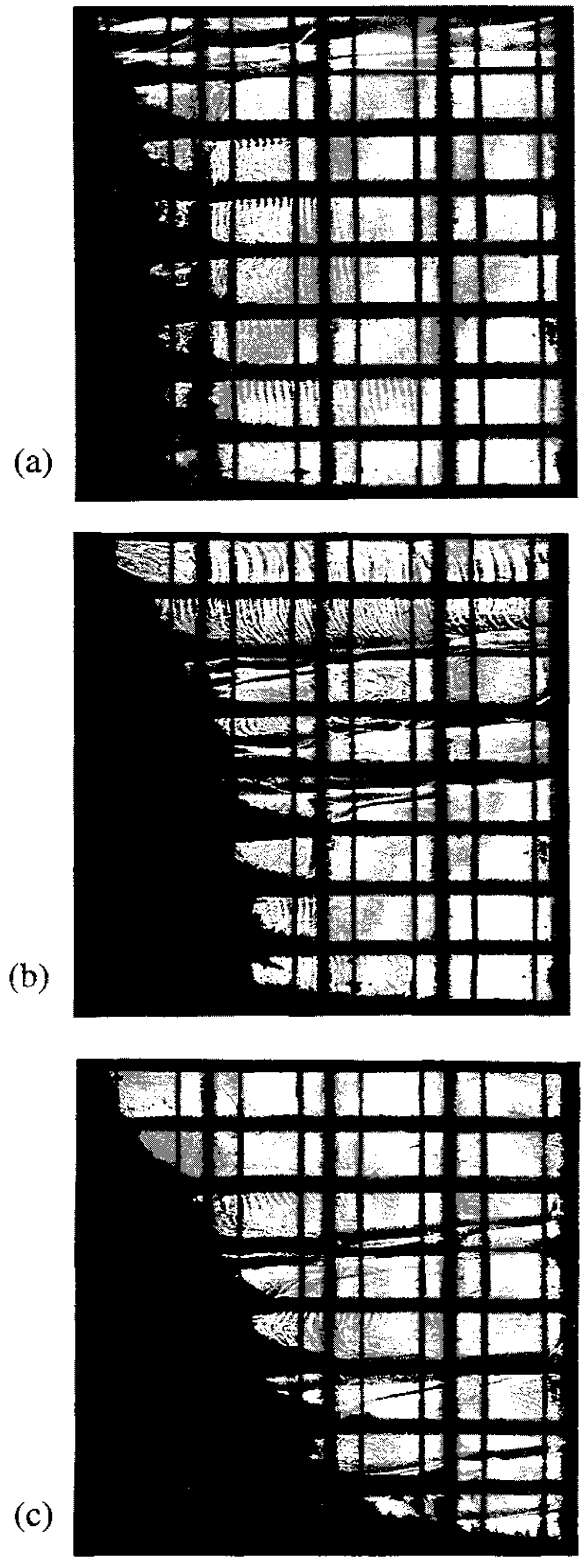

Fig. 5. Shadowgraph images taken during Experiment 2: (a) $t = 30$ min, (b) $t = 120$ min, and (c) $t = 240$ min.

dropped by a larger extent compared with the temperature drop. The temperature distributions in the middle and upper fluid layers were also fairly uniform and the transient changes were much smaller than those in the lower fluid layer (Fig. 4). The difference between the medium temperature and the equilibrium-liquidus temperature at $\xi = 0.07$ and $\eta = 0.93$ reversed at $t \approx 95$ min, as the growth of the primary solid phase ceased and remelting started to occur.

4.3. Experiments 2, 3 and 4: presence of porous matrix

The porous structure obstructed the migration of the separated crystals as well as the fluid motion during Experiment 2. Initially, the NH_4Cl crystals separated from the mushy region near the cold wall could not descend to the bottom wall but were captured by the porous plates surrounding the voids adjacent to the cold wall [24]. Unlike the single layer of mushy region grown from the separated crystals encountered in Experiment 1, which extended along the bottom, the buildup and growth of separated crystals occurred along the horizontal porous plates near the cold wall. The shapes of the rising water-rich plumes suggested that the cell-type flows developed within the voids near the cold wall. At $t = 30$ min (Fig. 5(a)), a couple of DDIs appeared below the top wall. As the primary solid phase growing around the second vertical porous plate from the cold wall linked the primary solid phase around the horizontal porous plates, the mushy and liquid regions were not simply connected. The growth of the primary phase within the voids between the second and third vertical porous plates from the cold wall was not active until the major portion of the voids next to the cold wall were filled with the mushy region. For the remaining duration of Experiment 2, the formation, motion and merging of DDIs were qualitatively the same as those observed in Experiment 1, where the porous structure was absent. However, the number of DDIs was larger in the presence of the porous matrix phase due to the reduced intensity of thermally driven flow, and the velocity of descending DDIs was greater due to the lower cold wall temperature and enhanced formation of the solid phases (Fig. 5(b) and 5(c)). After the liquid concentration in the top fluid layer reached about 21 wt% NH_4Cl ($\approx$100 min), no additional DDI (or fluid layer) formed, and the vertical extent of the fluid layers above the lowest DDI kept on increasing. The images of streak arrays, branched out from the horizontal porous plates found near the top wall in Fig. 5(b), were made when the DDI passed the horizontal porous plates and indicated that the mixing between the bulk fluid and remaining solution trapped by the porous matrix phase was not complete. The same type of images could be also made when the water-rich fluid

was swept through the horizontal porous plates by the thermally driven flow and were found around the porous plate near the mushy region.

The transient variation of the temperature and liquid concentration measured during Experiment 2 showed similar qualitative trends as those during Experiment 1. The horizontal distribution of the temperature and liquid concentration in the liquid region was less uniform compared with that in Experiment 1, since the advective transport of energy and species was reduced by the flow resistance offered by the porous structure. Similar to the data of Experiment 1, the medium temperatures measured in the liquid region were lower than the equilibrium liquidus temperatures (the medium was undercooled) below the lowest DDI, and were either higher than or almost equal to the equilibrium liquidus temperatures in the fluid layers above the lowest DDI. The undercooling of the interdendritic liquid also existed, but the extent was no larger than the ones in Experiment 1, despite the larger cooling rate caused by the lower cold wall temperature. Due to the different cold wall temperatures, a direct comparison of the measured concentrations was not made.

In Experiment 3, the test cavity was solidified under the same conditions as Experiment 2, except that the hot wall temperature was higher (40°C). Due to the intense thermal flow, the overall volume fractions of the solid phases were smaller and the formation of DDI was retarded in comparison with Experiment 2. The streak-type images found below the lowest DDI (Fig. 6(a)), suggest that a considerable amount of the water-rich fluid discharged into the liquid region was swept away from the liquidus interface and was mixing with the bulk liquid over the liquid region. Only one DDI persisted to the end of the run, and the liquid region was divided into two fluid layers having similar vertical extent at $t = 480$ min (Fig. 6(b)). The temperature of the medium in the mushy region closely matched the local equilibrium liquidus temperature during Experiment 3, indicating that the undercooling of the interdendritic liquid was substantially reduced. The undercooling of the bulk liquid in the liquid region did not occur.

The trends with time of the liquid concentration measured at three different heights along $\xi = 0.68$ are compared in Fig. 7. The time rate of the liquid concen-

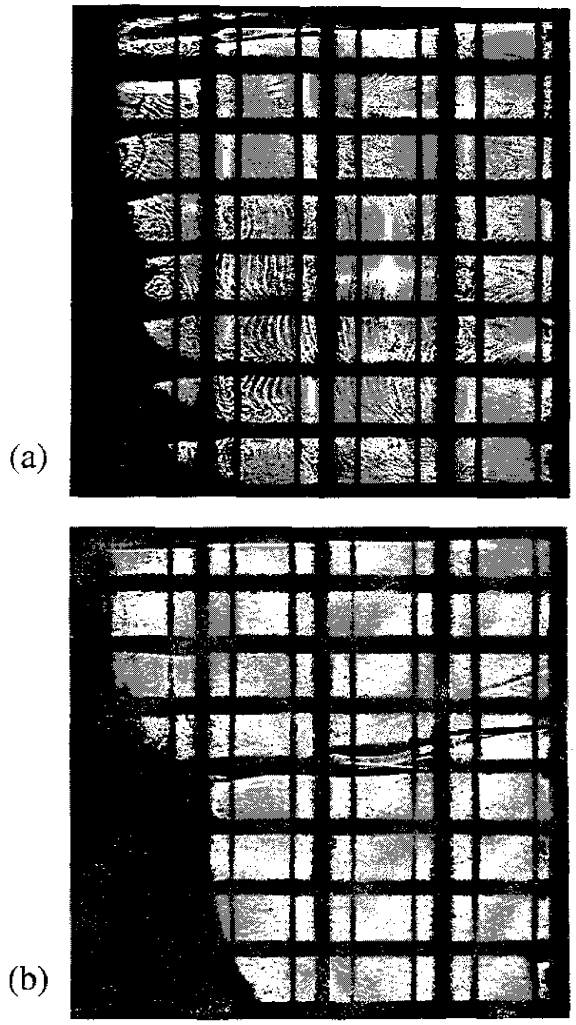

Fig. 6. Shadowgraph images taken during Experiment 3: (a) $t = 60$ min, and (b) $t = 480$ min.

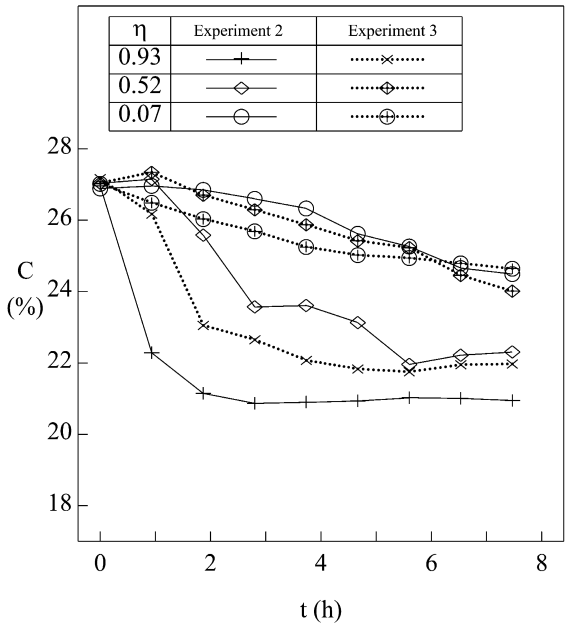

Fig. 7. Comparison of the measured concentration for Experiment 2 and 3 at $\xi = 0.68$.

tration change below the lowest DDI was almost constant for both cases but was larger when the thermal flow was relatively intense (Experiment 3). The decrease of the liquid concentration near the top wall ($\eta = 0.93$) was initially fast, but gradually decelerated with time as new DDIs ceased to form, and the vertical extent of the fluid layer just below the top wall started to increase. The overall decrease in the liquid concentration at $\eta = 0.93$ was smaller in Experiment 3 due to the smaller amount of solid phases formed. During Experiment 2, the liquid concentration at $\eta = 0.52$ and 0.07 rapidly approached the values at $\eta = 0.93$ whenever the DDI passed the measuring position. The amount of these decreases was larger at the higher measuring position ($\eta = 0.52$) for the same DDI and smaller for the higher DDI at the same measuring position. For Experiment 3 the measured liquid concentrations at $\eta = 0.52$ were slightly higher than those at $\eta = 0.07$ until the DDI passed the measuring position at $\eta = 0.52$.

The vertical distributions of the liquid concentration along $\xi = 0.68$ at $t = 480$ min are compared in Fig. 8. For both cases, the measured concentrations were fairly uniform within a given fluid layer. In Experiment 2, the difference in the liquid concentration across the higher DDI was larger compared with that across the lower DDI. The bright and dark strips in the shadowgraph images of the DDI were caused by the decrease and increase of the liquid concentration gradient across the DDI.

The experimental conditions for Experiment 4 were the same as those of Experiment 2, except that a different porous structure was employed. The permeability of the porous structure occupying the cavity in Experiment 4 was isotropic and it was about 50% smaller compared with the x-directional permeability (or about 90% of the y-directional permeability) of the porous structure employed. The number of DDI and the advance rate of the liquidus interface were greater in Experiment 4 due to the reduced thermal flow in the liquid region (compare Figs. 5 and 9), but the slope of the DDI increased as the horizontal permeability decreased by larger extent. The trends in the temperature and liquid concentration during Experiment 2 and 4 differed little from each other [24]. At all measuring locations, the liquid concentrations measured in Experiment 4 were closer to the eutectic composition as compared with those in Experiment 2, probably due to the larger amount of solid phases associated with the less intense thermal flow in the liquid region. However,

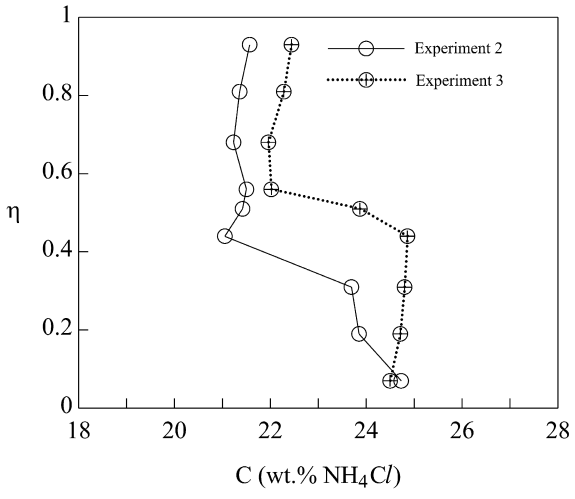

Fig. 8. Comparison of the measured concentration distributions for Experiment 2 and 3 along $\xi = 0.68$ at $t = 480$ min.

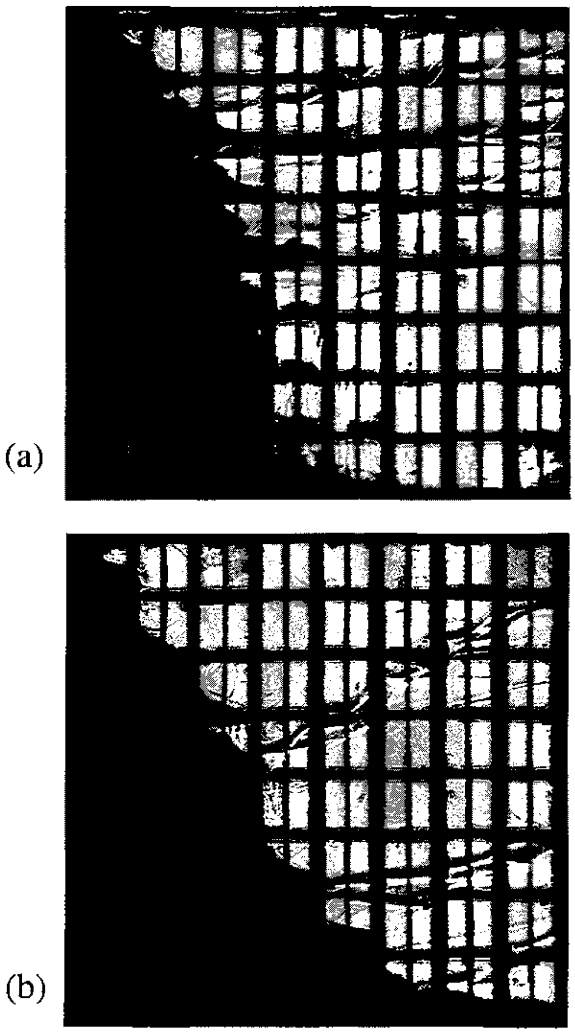

Fig. 9. Shadowgraph images taken during Experiment 4: (a) $t = 120$ min and (b) $t = 240$ min.

the differences between the measured liquid concentration, under the given change of the porous structure permeability, were generally smaller than the measurement uncertainty (5% of the reading).

The distribution of the measured liquid concentrations along the vertical line at $\xi = 0.68$ during Experiment 4 are presented in Fig. 10. According to the shadowgraph image in Fig. 9(a), each measuring position along the upper half of the line $\xi = 0.68$ belonged to different fluid layers, while those along the lower half were in the same fluid layer. The liquid concentration data indicated that the difference between the concentrations of the adjacent fluid layers was about the same at $t = 120$ min. The piecewise uniform profiles at later times ($t = 240$ and 480 min) confirmed that the vertical distributions of the liquid concentration were fairly uniform within a fluid layer, but the discrete changes in the liquid concentration existed across the DDIs [24]. The magnitude of the discrete change in the liquid concentration across the DDI increased from the bottom toward the top wall at later times. The average liquid concentration of a given fluid layer slowly increased with time.

4.4. Comparison of predicted and measured data

In order to validate the mathematical models, the conditions for Experiment 4 were numerically simulated and the predicted results compared with the experimental data. The thermophysical properties for the model input were the same as those in Table 2, except that all the phase densities were assumed to be the same and fixed at the value of 1082 kg/m^3.

The time evolution of streamlines predicted by the continuum porous medium model is shown in Fig. 11.

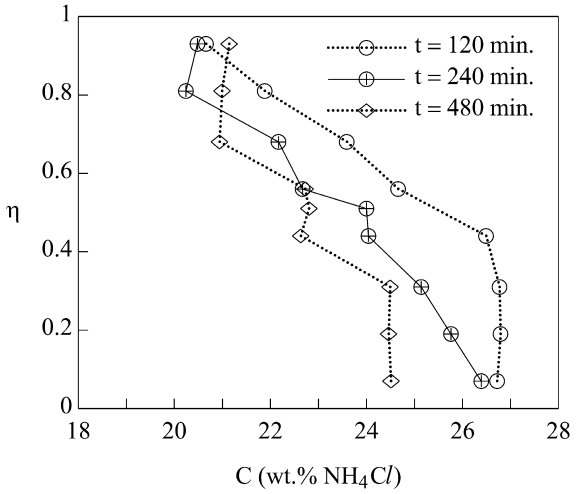

Fig. 10. Measured concentration distributions for Experiment 4 along $\xi = 0.68$.

During the first hour, the lower portion of the liquid region was occupied by the convection cell which was mainly driven by the thermal buoyancy forces, while the fluid motion in the mushy region and the upper portion of the liquid region was mainly driven by solutal buoyancy force, and the solutal convection cell existed across the liquidus interface. The vertical extent of the liquid region occupied by the thermal convection cell decreased with time, whereas that occupied by the solutal convection cell gradually increased. At $t =$ 2 h, a number of convection cells appeared above the solutal convection cell. The vertical extent of the liquid region containing these cells gradually increased, and the number of cells in this layer decreased as they merged. At later times, the thermal convection cell near the bottom and the solutal convection cell disappeared, in turn, and the liquid region was occupied by a single counter-clockwise rotating convection cell, which is mainly driven by the thermal buoyancy force. In the experiment, the solutal convection flow was less

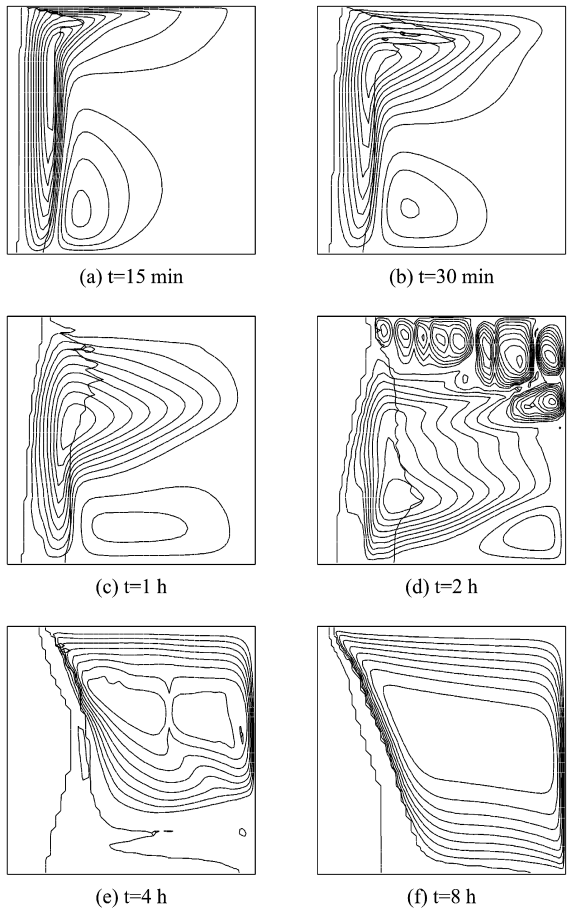

Fig. 11. Time evolution of predicted streamlines for Experiment 4 (equal increments).

stable, and the liquid region above the lowest thermal convection cell was divided into multiple double-diffusive layers. The remelting of the primary solid phase near the top started earlier and was greater in extent compared with the predictions. The horizontal extent of the mushy region near the top wall was thus overpredicted.

The predicted temperature profiles are compared with the experimental data in Fig. 12 at $t = 1$ h. A good agreement was obtained except near the top wall, where the temperature of the medium was underpredicted owing to the overprediction of discharge of the cold interdendritic liquid into the liquid region across the top portion of the liquidus interface. It is believed that the permeability of the mushy region in the direction normal to the primary arms was overestimated. The strong solutal stratification resulting from this vigorous discharge of interdendritic liquid into the liquid region may have suppressed the division of the liquid region into multiple double-diffusive layers which occurred in the experiment. Further research is needed concerning the flow structure resulting from the double-diffusive instability for more complete understanding of solidification of a solution.

A comparison of the predicted concentration distribution with experimental data along the vertical line at $\xi = 0.68$ also indicated that the discharge of interdendritic liquid into the liquid region was overpredicted (Fig. 13). The measured concentration profile at $t = 2$ h revealed the gradual variation between the initial concentration and the eutectic composition in the upper half of the liquid region, whereas the predicted profile had the uniform portion near the top wall for which the predicted concentration was within 2 wt% from the eutectic composition. At $t = 8$ h, the predicted concentration profile was uniform throughout the liquid region, while the measured values varied between 20% and 25%, due to the difference in the predicted and actual flow structure.

The discrepancy between the predictions and experimental data are partly due to the uncertainties in determining the flow characteristics of the dendrite array and partly due to the difference in the flow structure in the liquid region which has comparable temperature and concentration gradients in terms of equivalent buoyancy forces. For accurate prediction of mixture solidification, a dependable mathematical model which accounts for the dendritic permeability from the local solidification parameters within an acceptable uncertainty needs to be developed.

4.5. Effect of porous matrix flow characteristics

In order to investigate the effect of porous matrix flow characteristics on the predictions of solidification, numerical experiments were performed with the coefficients $R_{x,\,m}$ and $R_{y,\,m}$ as the variable parameters. The initial and boundary conditions of Experiment 4 were used, and the values of $R_{x,\,m}$ and $R_{y,\,m}$ were varied between 0.01 and 100 either simultaneously or individually.

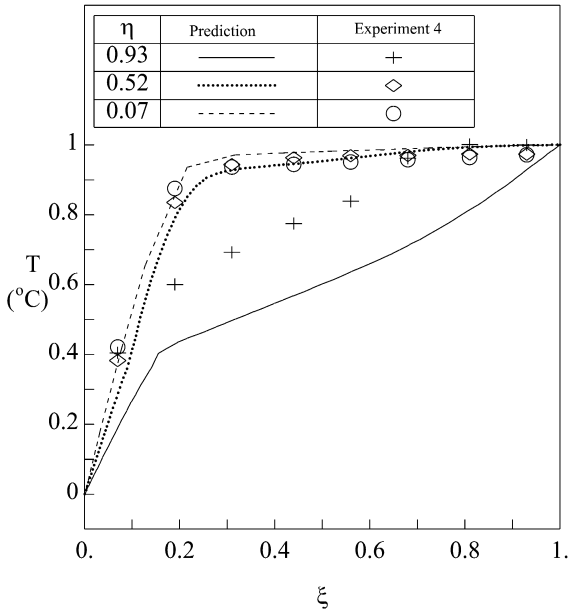

Fig. 12. Comparison between the predicted and measured temperature profiles at $t = 1$ h for Experiment 4.

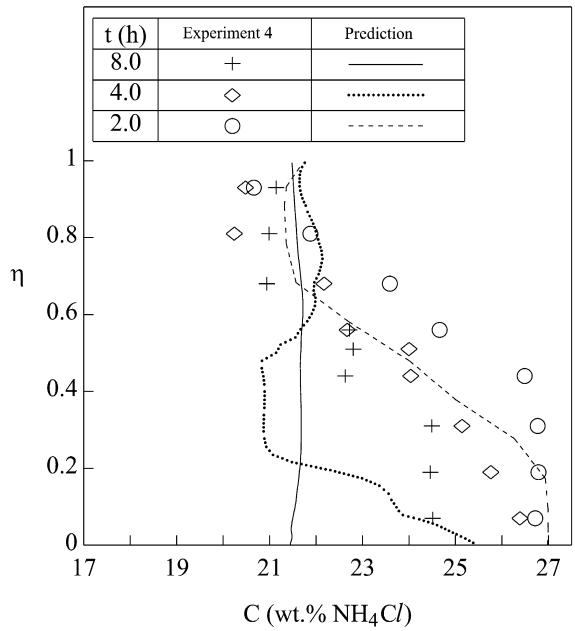

Fig. 13. Comparison of liquid concentration distributions along the vertical line at $\xi = 0.68$ for Experiment 4.

In Fig. 14 the predicted streamlines and isopleths of liquid concentration at $t = 4$ h for two extreme cases are contrasted to the intermediate one for which the permeability of the porous matrix phase was 8.368×10^{-9} (K_o). When the permeability of the porous matrix phase increased by the factor of 100, the distribution of the concentration in the liquid region was almost uniform, and the fluid motion was mainly driven by the thermal buoyancy force (Fig. 14(a)). The horizontal extent of the liquid region decreased toward the bottom due to the thermal stratification. The predicted macrosegregation pattern indicated that the composition of the solid region was fairly uniform except in the narrow region along the solidus interface near the bottom, whereas the strong positive segregation existed in the entire mushy region. This implies an active exchange of species between the mushy and liquid regions. The maximum local composition was close to unity, and the maximum was located in the middle of the mushy region just above the bottom. When the permeability of the porous matrix phase was smaller than K_o by two orders of magnitude, the solidus and liquidus interfaces were nearly vertical and the fluid motion was mainly driven by the solutal buoyancy force. The isopleths of liquid concentration (Fig. 14(c)) indicated that the influence of solutal convection on the distribution of liquid concentration was insignificant, and the solidification was almost unidirectional. A noticeable difference existed between the predicted macrosegregation when the porous matrix phase permeability decreased by two orders of magnitude from K_o. The entire medium within the enclosure had the average composition within ± 3.5 wt% from the initial composition, except for the small regions just above the bottom wall and just below the top wall. The maximum positive segregation waslocated just above the bottom wall and further away from the cold wall compared with those predicted with the higher porous medium permeability.

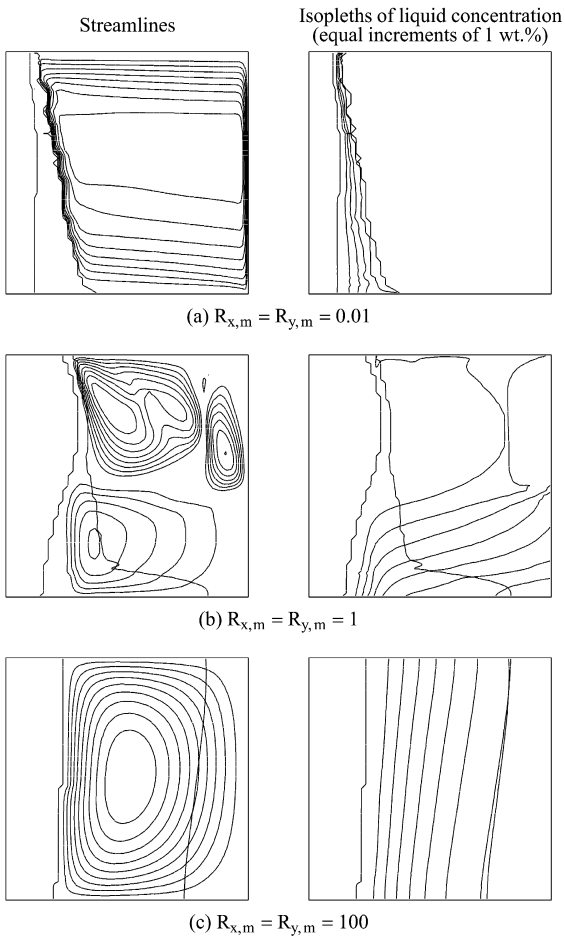

Fig. 14. Effect of porous matrix permeabilities on the flow streamlines (left panels) and liquid concentrations (right panels) for the conditions of Experiment 4.

The effect of dendritic permeability on the macrosegregation is quantified in terms of segregation quotient defined below:

$$S_Q = \left(\overline{\Delta C \varepsilon_{\alpha,\,\max}}\right)/\overline{\varepsilon}_\alpha \tag{29}$$

where

$$\overline{\Delta C} = \left(\sum |C - C_{in}| \rho \Delta V\right)/\sum \rho \Delta V \tag{30}$$

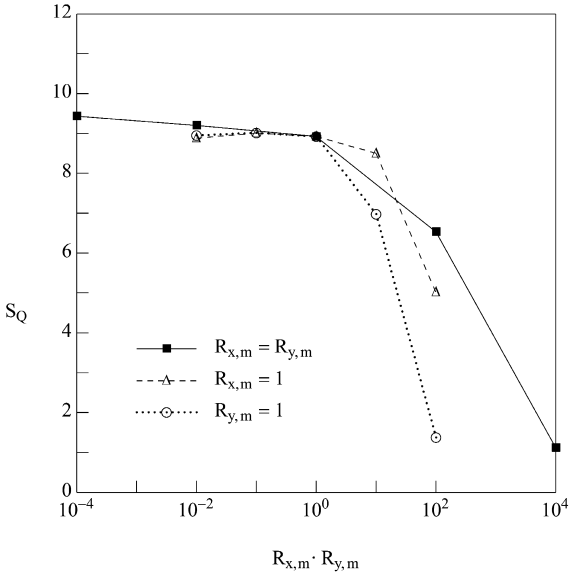

Fig. 15. Effect of porous matrix permeabilities on the segregation quotient for the conditions of Experiment 4.

$$\overline{\varepsilon}_\alpha = \left(\sum \varepsilon_\alpha \Delta V\right) / \sum \Delta V \tag{31}$$

$$\varepsilon_{\alpha,\,\max} = (C_{\text{in}} - C_{\text{eut}})/(C_\alpha - C_{\text{eut}}) \tag{32}$$

In the above equation, the $\overline{\varepsilon}_\alpha$ and $\varepsilon_{\alpha,\,\max}$ are defined to accommodate the effect of the incomplete solidification due to the presence of the hot wall. If an adiabatic thermal boundary condition is imposed at the vertical bounding wall opposite to the cold wall, the porous medium within the enclosure would solidify completely and the values of ε_α would be the same as $\varepsilon_{\alpha,\,\max}$. The predicted effect of porous matrix permeability on the segregation quotient is presented in Fig. 15. The most significant influence on the segregation quotient was caused by the decrease in the y-direction-permeability of the porous matrix. The decrease in the segregation quotient resulting from the simultaneous decrease in the permeabilities of the porous matrix in the x- and y-directions was almost equivalent to the change caused by the decrease of only the permeability in the y-direction by the same factor. The decrease in the porous matrix permeability in the x-direction also results in a comparable decrease of change in the segregation quotient. In contrast, the increase in the porous matrix permeability beyond the value of K_o did not cause any significant increase in the macrosegregation. Finally, the amount of macrosegregation occurring during the solidification of an off-eutectic composition solution can be reduced by placing a porous matrix phase. In order to obtain a significant decrease in the amount of macrosegregation, the permeability of the porous matrix phase must be smaller than the critical value, which is determined by the solutal buoyancy and viscous forces exerting on the melt, the dimension of the enclosure and the flow characteristics of the dendrite array. Under the conditions studied, the critical permeability of the porous matrix phase was about 8.37×10^{-9} (K_o). The amount of macrosegregation was insensitive to the permeability of the porous matrix phase smaller than this critical value and was mainly controlled by the porous matrix permeability in the gravity direction for the range larger than the critical value.

5. Conclusions

An experimental and analytical study on the lateral freezing of a porous medium saturated with an aqueous salt solution has been performed to obtain the improved understanding of the solute redistribution during phase change. Major attention was directed to the influence of the porous matrix phase on the interaction of hydrodynamics and advective heat and species transfer.

Solidification of an aqueous ammonium chloride solution was made to occur within a square cross-section test enclosure, which was cooled and heated at a pair of vertical end walls by imposing uniform but different temperatures. Artificial structures compatible with the flow visualization were constructed and served as the solid matrix of the porous medium. The flow structure in the liquid region was characterized by the double-diffusive interfaces and multiple fluid layers even in the presence of porous structure. When the porous structure was absent (Experiment 1), a considerable portion of the primary solid phase initially formed on the vertical cold wall separated and stranded along the bottom wall. The porous structure obstructed the migration of the crystals and offered an additional resistance to the motion of the fluid both in the liquid and mushy regions. The presence of the porous structure noticeably altered the distribution and the growth kinetics of the primary solid phase. When the hot wall temperature was lower and/or the permeability of the porous structure was smaller, the advance of the liquidus interface and the number of double-diffusive interfaces increased due to the reduced flow intensity in the liquid region.

Mathematical models based on heat and species conservation and relations from the phase diagram were suggested, and the predicted results for the representative conditions are compared with the experimental data. The discrepancy between the predictions and experimental data are partly due to the uncertainties in determining the flow characteristics of the dendrite array and partly due to the difference in the flow structure in the liquid region.

Parametric studies examining the effect of the flow characteristics possessed by the porous matrix phase were also conducted. The predicted amount of macrosegregation decreased when the permeabilities of the porous matrix phase decreased. In order to obtain a significant decrease in the amount of macrosegregation, the permeability of the porous matrix phase must be smaller than the critical value, which is determined by the solutal buoyancy and viscous forces exerting on the melt, the dimension of the enclosure and the flow characteristics of the dendrite array. Under the conditions studied, the critical permeability of the porous matrix phase was approximately 8.37×10^{-9} (K_o). The amount of macrosegregation was insensitive to the permeability of porous matrix phase smaller than this critical value, and was mainly controlled by the porous matrix permeability in the gravity direction for the range larger than the critical value.

References

[1] R. Viskanta, Phase change heat transfer in porous

media, in: Z.P. Zarling (Ed.), Third International Symposium on Cold Regions Heat Transfer, University of Alaska, Fairbanks, AK, 1991, pp. 1–24.
[2] R. Viskanta, M.V.A. Bianchi, J.K. Critser, D. Gao, Solidification process of solutions, Cryobiology 34 (1997) 348–362.
[3] Z.W. Cao, D. Poulikakos, Freezing of a binary alloy saturating a packed bed of spheres, Journal of Thermophysics and Heat Transfer 5 (1991) 46–53.
[4] M. Okada, M. Murakami, Solidification of porous media saturated with aqueous solution in a rectangular cell, in: 27th National Heat Transfer Symposium of Japan, Heat Transfer Society of Japan, Tokyo, Japan, 1998, pp. 241–243.
[5] K. Matsumoto, M. Okada, Y. Murakami, Y. Yabushita, Solidification of porous medium saturated with aqueous solution in a rectangular cell, International Journal of Heat and Mass Transfer 36 (1993) 2869–2880.
[6] M. Song, J. Choi, R. Viskanta, Upward solidification of a binary solution saturated porous medium, International Journal of Heat and Mass Transfer 15 (1993) 3687–3695.
[7] J. Choi, R. Viskanta. Freezing of aqueous sodium chloride solution saturated packed bed from above, in: E. Toner (Ed.), Topics in Heat Transfer, ASME, New York, HTD-vol. 206-2, pp. 159–166.
[8] M. Okada, M. Ochi, M. Tateno. Solidification of a supercooled aqueous solution in a porous medium, in: J.S. Lee (Ed.), Proceedings of the 11th International Heat Transfer Conference, KSME, Korea, vol. 7, pp. 169–174.
[9] M. Song, R. Viskanta, Flow characteristics of anisotropic structures constructed with porous layers, Transport in Porous Media 15 (1994) 151–174.
[10] R. Viskanta, Transport phenomena during solidification of binary systems, in: L.F.A. et al. Azevedo (Ed.), Proceedings of the 4th Brazilian Thermal Science Meeting, Brazilian Society of Mechanical Engineers, Rio de Janeiro, 1992, pp. 39–50.
[11] M.W. Zemanski, R.H. Dittman, Heat and Thermodynamics, McGraw-Hill, New York, 1981.
[12] W. Kurz, D.J. Fisher, Fundamentals of Solidification, Trans Tech Publication, Switzerland, 1989.
[13] M. Song, R. Viskanta, Electrochemical method to measure the composition of the liquid phase during the solidification of NH_4Cl–H_2O system, Review of Scientific Instruments 66 (1995) 4336–4340.
[14] C. Beckerman, R. Viskanta, Modeling transport during alloy solidification, Applied Mechanics Reviews 46 (1993) 1–26.
[15] R.M. Fand, B.K.Y. Kim, A.C.C. Lam, R.T. Phan, Resistance to the flow of fluids through simple and complex porous media whose matrices are composed of randomly packed spheres, Journal of Fluids Engineering 109 (1998) 268–274.
[16] S.D. Felicelli, J.C. Heinrich, D.R. Poirier, Simulation of freckles during vertical solidification of binary alloys, Metallurgical Transactions 22B (1991) 847–859.
[17] D.R. Poirier, Permeability for flow of interdendritic liquid in columnar dendritic alloys, Metallurgical Transactions 18B (1987) 245–255.
[18] K. Somboonsuk, J.T. Mason, R. Trivedi, Interdendritic spacing: Part I. Experimental studies, Metallurgical Transactions 15A (1984) 967–975.
[19] R. Trivedi, Interdendritic spacing: Part II. Comparison of theory and experiment, Metallurgical Transactions 15A (1984) 977–982.
[20] Doormaal, J.P. Van, G.D. Raithby, Enhancements of the SIMPLE method for predicting incompressible fluid flow, Numerical Heat Transfer 7 (1984) 147–163.
[21] D. Morrow, B. Holter, A vectorized polynomial preconditioned conjugate gradient solver package for the USGS 3D ground-water model, in: M. Strech (Ed.), Proceedings of the 15th Annual Water Resources Conference, American Society of Civil Engineers, New York, 1988, pp. 321–324.
[22] M. Schäfer, Parallel algorithms for the numerical simulation of three-dimensional natural convection, Applied Numerical Mathematics 7 (1991) 347–365.
[23] H.L. Stone, Iterative solution of implicit approximations of multidimensional partial differential equations, SIAM Journal of Numerical Analysis 5 (1968) 531–559.
[24] M. Song. Solidification of an anisotropic porous medium saturated with a binary alloy, Ph.D. thesis, Purdue University, West Lafayette, IN, 1995.
[25] C. Beckermann. Melting and solidification of binary mixtures with double diffusive convection in the melt, Ph.D. thesis, Purdue University, West Lafayette, IN, 1987.
[26] M.S. Christenson, F.R. Incropera, Solidification of an aqueous ammonium chloride solution in a rectangular cavity — I. Experimental study, International Journal of Heat and Mass Transfer 32 (1989) 47–68.